AGU ADVANCING EARTH AND SPACE SCIENCE

Geophysical Research Letters®

RESEARCH LETTER
10.1029/2023GL103790

A Cloud-Free Approach to Modeling Daily Downwelling Longwave Irradiance at Global Scale

Ryan M. Bright[1] and **Stephanie Eisner**[1]

[1]Division of Forestry and Forest Resources, Department of Forests and Climate, Norwegian Institute of Bioeconomy Research (NIBIO), Ås, Norway

Key Points:

- A model free of cloud variables or their solar-based proxies is proposed to correct clear-sky longwave irradiances under all-sky conditions
- Model performance is weakly sensitive to the underlying clear-sky model when jointly parameterized
- The model yields daily errors of 3.9%–4.5% over ocean and 5.5%–7% over land, depending on the error metric and underlying clear-sky model

Supporting Information:

Supporting Information may be found in the online version of this article.

Correspondence to:

R. M. Bright,
ryan.bright@nibio.no

Citation:

Bright, R. M., & Eisner, S. (2023). A cloud-free approach to modeling daily downwelling longwave irradiance at global scale. *Geophysical Research Letters*, *50*, e2023GL103790. https://doi.org/10.1029/2023GL103790

Received 21 MAR 2023
Accepted 3 JUN 2023

Author Contributions:

Conceptualization: Ryan M. Bright, Stephanie Eisner
Formal analysis: Ryan M. Bright
Funding acquisition: Stephanie Eisner
Methodology: Ryan M. Bright
Writing – original draft: Ryan M. Bright
Writing – review & editing: Ryan M. Bright, Stephanie Eisner

Abstract Parametric modeling of downwelling longwave irradiance under all-sky conditions ($LW_{\downarrow}$) typically involves "correcting" a clear- (or non-overcast) sky model estimate using solar-irradiance-based proxies of cloud cover in lieu of actual cloud cover given uncertainties and measurement challenges of the latter. While such approaches are deemed sound, their application in time and space is inherently limited. We report on a correction model free of solar irradiance-derived cloud proxies that is applicable at the true daily (24 hr) and global scales. The new "cloud-free" correction model demonstrates superior performance in a range of environments relative to existing cloud-free modeling approaches and to corrections based on solar-derived cloudiness proxies. Literature-based performance benchmarking indicates a performance that is often comparable to—and in some cases superior to—performances yielded by conventional parametric modeling approaches employing locally or regionally calibrated parameters, as well as to performances of satellite-based algorithms.

Plain Language Summary Downwelling longwave irradiance ($LW_{\downarrow}$) is a major component of Earth's surface energy budget and is often modeled indirectly using routinely measured surface meteorological variables. In overcast (or "all-sky") conditions, $LW_{\downarrow}$ is typically estimated by correcting an estimate valid for non-overcast (or "clear-sky") conditions using information about cloud cover or cloudiness proxies derived from solar irradiance variables. Cloud cover information is often unavailable and uncertain, and proxies based on solar irradiance variables inherently limit the correction to the daytime. Here, we present a correction model that circumvents the dependence on cloud variables or their proxies and document its performance when applied under a variety of conditions.

1. Introduction

Downwelling longwave irradiance ($LW_{\downarrow}$) is an essential climate variable (Bojinski et al., 2014) for determining the energy balance at Earth's surface and hence in the calculation of surface heat and moisture fluxes. Unlike solar (shortwave) irradiance, however, $LW_{\downarrow}$ is challenging and expensive to measure (Castro Aguilar et al., 2015) and is often estimated indirectly with parametric modeling of routinely measured surface-level meteorological variables (Sridhar & Elliott, 2002). While many satellite-based $LW_{\downarrow}$ estimation algorithms exist with newer ones indicating great promise (Letu et al., 2022; Riihelä et al., 2017; Zeng et al., 2020; Wang et al., 2020), they remain challenging to apply at point scale and in a prognostic manner. Estimates from simplified parametric models are widely applied and heavily desired in a wide range of applications (Wang & Liang, 2009; Wang & Dickinson, 2013) and are the sole focus of the present work.

Under non-overcast or "clear-sky" (CS) conditions, $LW_{\downarrow}$ is primarily influenced by water vapor and air temperature near the surface (Brutsaert, 1975; Shakespeare & Roderick, 2021). As such, parametric models for estimating longwave irradiance during clear-sky conditions (henceforth $LW_{0\downarrow}$) often rely on screen-level measurements of temperature and humidity (Flerchinger et al., 2009). Under cloudy or "all-sky" (AS) conditions, however, cloud water droplets and ice crystals represent additional emitters that complicate $LW_{\downarrow}$ estimation and typically serve to increase $LW_{\downarrow}$ over $LW_{0\downarrow}$ (Arking, 1991; Kondratyev, 1969; Yamanouchi & Kawaguchi, 1984). Various models have been proposed to correct for this increase by incorporating cloud covered area fraction (f_c) or cloudiness proxies based on the clearness index (i.e., $SW_{\downarrow}/SW_{\downarrow,TOA}$) or fractional clear-sky solar irradiance (i.e., $SW_{\downarrow}/SW_{0,\downarrow}$; see the review by Flerchinger et al. (2009) for a thorough overview here). Regarding the former, f_c is rarely measured in the field and is subject to human error or subjectivity when it is (Gubler et al., 2012; Liu et al., 2018; Marty & Philipona, 2000). And while cloud properties including f_c can be obtained from satellite remote sensing,

their spatial and temporal resolutions may be too coarse for many applications (Riihelä et al., 2017; Wang & Dickinson, 2013). Thus, clear-sky correction models (CSCMs) based on solar-derived cloudiness proxies (f_c*) prevail overwhelmingly in the literature and typically lead to lower estimation error than those employing f_c (Flerchinger et al., 2009).

However, the reliance on f_c* severely limits a CSCM's applicability in time and space. In terms of daily (24-hr mean) $LW_{\downarrow}$ modeling, such a correction requires assuming that daylight conditions are representative of the daily mean, or approximating nocturnal cloudiness using the cloudiness index from the daylight envelope—both of which can be particularly problematic for regions experiencing large diurnal-nocturnal asymmetries in cloud cover over the diel cycle (Cox et al., 2020; Dai et al., 1999). This may explain why, as a daily model, none of the f_c*-based algorithms reviewed by Flerchinger et al. (2009) sufficiently captured the diurnal variation around the daily average. This same solar irradiance dependency also renders f_c*-based CSCMs inapplicable in polar regions during winter due to the lack of sunlight for prolonged periods—regions where there is an increasing need for reliable $LW_{\downarrow}$ estimates (Riihelä et al., 2017). Thus, a daily CSCM that is truly global must either rely on f_c or on non-solar-derived variables that strongly co-vary with cloud radiative properties in time and space.

Here, we present a true daily and globally applicable CSCM that neither depends on f_c* nor f_c given the drawbacks described above. Its performance was rigorously assessed when applied to correct $LW_{0\downarrow}$ estimates emanating from three leading parametric and one semi-analytical clear-sky models. Our performance evaluation relied on both *in-situ* and global reanalysis benchmarks—the latter being motivated by the desire to assess performance over ocean surfaces, which is often overlooked in model evaluation studies. Performance was subsequently benchmarked to $LW_{\downarrow}$ estimates stemming from three standalone all-sky models and a leading f_c*-based CSCM where applicable. Readers are referred to the reviews by Flerchinger et al. (2009), Wang and Liang (2009), Wang and Dickinson (2013), Cheng et al. (2019), and Guo et al. (2019) for detailed descriptions of the prevailing parametric models along with their accuracies.

2. A Cloud-Free CSCM

The functional form of two widely applied CSCMs can be generalized (Carmona et al., 2014; Duarte et al., 2006; Pirazzini et al., 2000) as follows:

$$LW_{\downarrow} = (1 - N^{\mu})LW_{0,\downarrow} + N^{\mu}\sigma T_a^4 \quad (1)$$

$$LW_{\downarrow} = \left(1 + \alpha N^{\beta}\right)LW_{0,\downarrow} \quad (2)$$

where $LW_{0\downarrow}$ is the longwave irradiance estimate from a clear-sky model (W m^{-2}) evaluated at the air temperature near the surface (T_a; K), σ is Stefan-Boltzmann's constant (= 5.678×10^{-8} W m^{-2} K^{-4}), N is f_c or f_c*, and α, β, and μ are fit parameters. To our knowledge there does not exist a CSCM that does not assume f_c or f_c* as N. Equation 1 is often deemed the better model due to its stronger physical basis (Duarte et al., 2006)—which is that $LW_{\downarrow}$ originates from the cloud base under overcast skies (i.e., when $N = f_c = 1$) when the emissivity from the air column determining $LW_{0,\downarrow}$ is rendered ineffective (Konzelmann et al., 1994). Note that Equation 1's form when excluding μ resembles the Crawford and Duchon (1999) model whose strength and superiority has been showcased by several authors (Carmona et al., 2014; Cheng et al., 2019; Choi, 2013; Flerchinger et al., 2009; Lhomme et al., 2007; Wang & Liang, 2009).

Given the strong relationship between cloud cover and RH (Chepfer et al., 2019; Sicart et al., 2006; Sundqvist, 1978; Walcek, 1994), we sought to identify a CSCM employing RH in lieu of f_c or f_c*. It became evident when examining our training data (Section 3) that the magnitude of the correction (or the quotient of $LW_{\downarrow}/LW_{0,\downarrow}$) generally displayed a power law relationship with RH—albeit with significant noise. Considering that $LW_{0,\downarrow}$ is a strong function of the air temperature near the surface (i.e., $LW_{0\downarrow} = \varepsilon_0\sigma T_a^4$), the magnitude of the correction for a given RH must be smaller when $LW_{0,\downarrow}$ is already large—or when the air temperature (T_a) is already high. Given this, we were able to reduce this noise after further considering the modifying effect of T_a—and even further still when considering instead the water vapor holding capacity of air near the surface (i.e., the saturated water vapor pressure; e_s)—a surprising outcome given that e_s is a function of T_a only. In other words, corrections for a given RH became smaller (larger) as e_s (or T_a) became larger (smaller). We then sought to encapsulate this relationship within the correction models presented as Equations 1 and 2, finding Equation 1 to yield better results judging by

Table 1
Models Selected for Inclusion in the Calibration and Performance Evaluation Exercises

Model ID	Model	Constants or empirical parameters[a]	Reference
Clear-sky models			
S&R21-CS	$LW_{0,\downarrow} = (1 - e^{-\tau})\sigma T_a^4$	$\tau = f(H_e, CO_2, q_a); H_e = f(H, P_a, P_0, m, \theta_r); CO_2 = 400$ ppmv; $P_0 = 101$ kPa; $m = 1.8$; $\theta_r = 40.3°$	(Shakespeare and Roderick (2021))
B32-CS	$LW_{0,\downarrow} = \left(k_1 + k_2\sqrt{e_a}\right)\sigma T_a^4$	$k_1 = 0.5856; k_2 = 0.0525$	(Brunt (1932))
B75-CS	$LW_{0,\downarrow} = \left[k_1 (e_a/T_a)^{k_2}\right]\sigma T_a^4$	$k_1 = 1.0397; k_2 = 0.0890$	(Brutsaert (1975))
C14-CS	$LW_{0,\downarrow} = (k_1 + k_2 T_a + k_3 \mathrm{RH})\sigma T_a^4$	$k_1 = -0.4677; k_2 = 0.0038; k_3 = 0.0022$	(Carmona et al. (2014))
All-sky models (standalone)			
A12-AS	$LW_{\downarrow} = k_1 + k_2 e_a + k_3 T_a$	$k_1 = -594.58; k_2 = 2.9051; k_3 = 3.0967$	(Abramowitz et al. (2012))
C&Z19-AS	$LW_{\downarrow} = \left[k_1 + k_2 \mathrm{FRH} + k_3 \ln(e_a/T_a)\right]\sigma T_a^4$	$k_1 = 0.7611; k_2 = 0.2578; k_3 = 0.0277$	(Chang and Zhang (2019))
New-AS	$LW_{\downarrow} = \left[k_1 + k_2 \mathrm{ALT} + k_3 e^{(k_4 \mathrm{FRH})} + k_5 \ln(e_a/T_a)\right]\sigma T_a^4$	$k_1 = 0.8219; k_2 = -1.5300 \times 10^{-5}; k_3 = 0.0152; k_4 = 2.7235; k_5 = 0.0247$	This study

Note. "τ" = effective optical depth (unitless); "H_e" = effective water vapor scale height (m); "q_a" = specific humidity at 2 m above surface (kg kg^{-1}); "CO_2" = global mean CO_2 concentration (ppmv); "H" = water vapor scale height–or the ratio of total column water vapor to the water vapor density at the surface (unitless); "P_a" = air pressure at 2 m above surface (hPa); "P_0" = reference surface pressure (hPa); "θ_r" = representative angle (°); "m" = empirical parameter; "e_a" = water vapor pressure at 2 m above surface (hPa); "T_a" = air temperature (dry bulb) at 2 m above surface (K); "RH" = relative humidity (%); "FRH" = fractional relative humidity (RH/100; unitless); "ALT" = geometric altitude (m.a.s.l.). "σ" = Stefan-Boltzmann's constant (=5.678 × 10^{-8} W m^{-2} K^{-4}).
[a]Parameter values are based on least squares regressions of daily ERA5 (see Section 3.1).

several performance metrics (i.e., R^2, RMSE, ΔAIC) obtained via non-linear least squares regressions.

One could think of N in Equation 1 as the emissivity of clouds rather than cloud (area) fraction or its solar-based proxy. Re-writing Equation 1 in terms of clear- and all-sky emissivities (ε_0 and ε_a, respectively) and denoting the term N^{μ} as a single variable x, we obtain:

$$LW_{\downarrow} = \varepsilon_a \sigma T_a^4 = (1 - x)\varepsilon_0 \sigma T_a^4 + x\sigma T_a^4 \tag{3}$$

which collapses to:

$$\varepsilon_a = \varepsilon_0 - x\varepsilon_0 + x \tag{4}$$

Re-arranging and solving for x gives:

$$x = \frac{\varepsilon_a - \varepsilon_0}{1 - \varepsilon_0} \tag{5}$$

where x emerges as a variable analogous to the "cloud effective emissivity" term $\varepsilon_{\mathrm{eff}}$ defined in Liu et al. (2018):

$$\varepsilon_{\mathrm{eff}} = \frac{LW_{\downarrow} - LW_{0,\downarrow}}{LW_{\mathrm{BB},\downarrow} - LW_{0,\downarrow}} = \frac{\varepsilon_a - \varepsilon_0}{1 - \varepsilon_0} = x \tag{6}$$

where $LW_{\mathrm{BB},\downarrow}$ is the black-body irradiance.

Hence by replacing the cloud term N^{μ} with RH and adding shape and power parameters modulated by e_s, we essentially obtained a model for $\varepsilon_{\mathrm{eff}}$:

$$\varepsilon_{\mathrm{eff}} = (k_1 + k_2 e_s)\mathrm{FRH}^{(k_3 + k_4 e_s)} \tag{7}$$

whose parameters were obtained when fitting the full CSCM:

$$LW_{\downarrow} = (1 - \varepsilon_{\mathrm{eff}})LW_{0,\downarrow} + \varepsilon_{\mathrm{eff}}\sigma T_a^4 \tag{8}$$

where FRH is fractional RH (= RH/100), e_s is the saturated water vapor pressure (in hPa) evaluated at the surface air temperature (Buck, 1981), and k_n are fit parameters that depend on the underlying clear-sky model. Because this correction does not represent cloud coverage explicitly—only implicitly through RH and the modulating effect of water vapor holding capacity near the surface—we refer to Equations 7 and 8 as our "cloud-free" CSCM. Refer to Table S1 in Supporting Information S1 for parameter values and fit summary statistics, Figure S1 in Supporting Information S1 for an illustration of the behavior of the $\varepsilon_{\mathrm{eff}}$ model (i.e., Equation 7), and Equation S1 in Supporting Information S1 for the full model expression.

3. Data and Methods

Our workflow is succinctly outlined as follows: (a) clear-sky model selection and calibration; (b) all-sky model calibration; (c) performance evaluation based on global climate model reanalysis; (d) performance evaluation based on *in-situ* observations.

3.1. Clear-Sky Model Selection and Calibration

Three parametric and one semi-analytical model of $LW_{0\downarrow}$ were chosen (Table 1) after an extensive literature review (see Text S1 in Supporting Information S1 for a short rationale). To equitably evaluate and robustly

compare model performances, we needed to ensure that each model's parameters (Table 1) were calibrated to the same data sample. The calibration based on non-linear least squares regression was performed on daily averages of the hourly ERA5 global reanalysis product (Hersbach et al., 2020) for the year 2016. We defined clear-sky days as days whose $LW_{\downarrow}/LW_{0,\downarrow}$ quotient was less than 1.025. ERA5 was chosen over satellite-based products such as CERES-SYN (Rutan et al., 2015) given its higher spatial resolution (=larger sample size) and better agreement with observations at the daily resolution (Feng et al., 2021; Tang et al., 2021). Further, ERA5 preserves a physical consistency between candidate model input variables and $LW_{\downarrow}$.

Warmer and drier regions were greatly overrepresented in the resulting clear-sky data set. We therefore created 5 W m^{-2} bins and drew a random sample of 200,000 days from each bin falling within the inner-90th percentile of the data range. The resulting uniform distribution based on $LW_{0,\downarrow}$ flux magnitude ensured a more even spatial distribution, confirmed upon visual inspection after re-mapping remaining retained data points (days) back to the ERA5 grid (0.25° × 0.25°; see Figure S2 in Supporting Information S1). This approach enabled a large global coverage, albeit with gaps located in the notoriously overcast regions of the Southern Ocean, the northeast Pacific, and the north Atlantic. Fit summary statistics are provided in Table S2 in Supporting Information S1.

3.2. All-Sky Model Calibration

We calibrated our CSCM to a random 10-day sample (yielding a total of 10.38×10^6 days for the 0.25° × 0.25° spatial resolution grid) using the $LW_{0,\downarrow}$ estimates from the four clear-sky models presented in Table 1, retaining the parameters calibrated on the clear-sky sample described above for the three parametric models ("B32"; "B75"; "C14"). We checked for the influence of sampling bias by repeating the fitting process after expanding the training sample first to 20- ($n = 20.76 \times 10^6$ days) and then to 30 random days ($n = 31.15 \times 10^6$ days). Parameter values, goodness-of-fits (χ^2), and other fit summary measures (RMSE; R^2) remained stable regardless of the sample size, thus ensuring the 10-day sample was free from temporal sampling bias.

Performances of the four CSCM-CS model variants were compared to all-sky estimates emanating from two existing and one new standalone parametric models (Table 1). Parameters for the two existing models ("A12"; "C&Z19"; see Text S1 in Supporting Information S1 for details) were calibrated on the same 10-day sample as the four CSCM variants. We further considered a new standalone model given the redundancy issue reported by Li et al. (2017) and the concern that our CSCM might not yield an improved performance over a standalone model given the high multicollinearity between input variables of the clear-sky models (Table 1) and the CSCM (Equations 7 and 8). The functional form of this model ("New-AS," Table 1) was the result of experimentation with existing variable relationships seen in other models. The model included an $\ln(e_s/T_a)$ term like the C&Z19-AS model but differed with respect to the relationship with relative humidity (exponential vs. linear) as well as the inclusion of an altitude correction, the latter being motivated by findings reported elsewhere (Cheng et al., 2019; Yang et al., 2010).

3.3. Performance Evaluation Based on ERA5

Many previous studies assessed model performance by comparing to $LW_{\downarrow}$ observations measured *in-situ* using pyrgeometers based on land. As such, there remains a gap in our understanding about the performances of prevailing models over ocean, where large application needs remain (di Sarra et al., 2019; Ghate et al., 2009). Further, stations within *in-situ* networks were unevenly distributed in space, which could bias the evaluation. We therefore elected to employ the ERA5 data set also as part of our performance evaluation to expand coverage in both time and space. Given our finding that model parameters and goodness-of-fits remained relatively insensitive to changes to the sample size and make-up, and because the training samples represented only a very minor proportion of the full data set (~10 and ~15 of ~380 million days for the all- and clear-sky training samples, respectively), we deemed it justifiable to include the training day sample when evaluating model performances.

Apart from the distinction between land and ocean surfaces, we assessed performance under both cold and high-altitude conditions given previous findings surrounding degraded model performances at low temperatures (Gubler et al., 2012) and high altitudes (Cheng et al., 2019). In total, performance metrics were computed for the full globe (all grid cells and days in 2016) and the following four subsets: (a) HIGH—all days for grid cells having a mean altitude of >1,500 m.a.s.l; (b) COLD—all days of any grid cell having a daily mean air temperature (2 m) of <273 K; (c) OCEAN—all days for grid cells classified as ocean in the ERA5 land-ocean mask; and (d) LAND—all days for grid cells classified as land.

Performance was assessed using standard performance metrics such as RMSE and mean absolute error (MAE). Details on metric calculation are elaborated in Text S2 in Supporting Information S1.

3.4. *In-Situ* Performance Evaluation on Land

To assess the robustness of the ERA5-calibrated model parameters and strengthen the performance evaluation, we employed a second evaluation data set comprising 247,933 daily $LW_{\downarrow}$ observations measured *in-situ* at 55 sites in BSRN (Driemel et al., 2018) and 75 sites in the FLUXNET2015 synthesis data set (Pastorello et al., 2020). Site names and locations are provided in Figures S3 and S4 in Supporting Information S1, respectively. Quality assessment and filtering procedures are described in Text S3 in Supporting Information S1. The same performance metrics presented above were computed for the full daily *in-situ* record and the following subsets: (a) HIGH—all days for sites with an altitude of >1,500 m.a.s.l; (b) COLD—all days having a daily mean air temperature (2 m) of <273 K; (c) BSRN—all days for sites in BSRN; and (d) FN15—all days for sites in the FLUXNET2015 data set. The partitioning by network was motivated by reported quality differences (Wang & Dickinson, 2013). Lastly, to equitably compare to the Crawford and Duchon (1999) CSCM based on f_c*, we created a final subset based on all days having 24 hr of daylight.

4. Results

Starting with the ERA5-based performance assessment, all model variants employing the new CSCM exhibited a superior performance over the two existing standalone models irrespective of the subset (Figure 1d). Judged globally, performances of the four CSCM variants varied little, with the B32 and S&R21 variants yielding the lowest RMSE and MAE of 5.1% and 4.2%, respectively (Figure 1d, "Global"), which may be contrasted to RMSEs of 6.5% and 5.5% and MAEs of 5.5% and 4.6% yielded by the standalone models of Abramowitz et al. (2012) and Chang and Zhang (2019), respectively. Among the four variants employing the new CSCM, the B32 variant yielded lowest errors over land (Figure 1d, "Land") while the S&R21 variant yielded lowest errors over ocean (Figure 1d, "Ocean"), which is likely attributable to the superiority of the underlying clear-sky models under these same conditions (Table S3 in Supporting Information S1). The worst performances for all models were seen at the higher altitudes (Figure 1d, "HIGH") where the new standalone model ("New-AS") with its altitude correction performed slightly better than the four new CSCM variants. Relatively poor performances were also found by all models for cold days and locations, where the B32 variant yielded lowest errors (Figure 1d, "COLD"). Globally, the performance of "New-AS" was on par with the four CSCM variants.

While RMSEs and MAEs among the four CSCM variants varied little overall for any given subset, differences in relative error distributions were evident (Figure 1b). At LAND and HIGH subsets, for instance, errors of the B32 variant were more positively biased, whereas errors for both the B32 and S&R21 variants were more negatively biased at OCEAN and COLD subsets. Globally, errors of the B75 variant were found to be the most normally distributed of all four CSCM-based variants.

Clear differences between the four CSCM variants emerged upon inspection of the spatial distribution of RMSE (Figures 1a and 1c). The S&R21 variant yielded the lowest RMSE over the largest proportion of area (27%; Figure 1c), owed to its superior performance over ocean in the northern hemisphere (Figure 1a). Of the four CSCM variants, the B32 variant yielded the lowest RMSE over the second largest proportion of area (17.5%), which was more evenly distributed between land (9.5%) and ocean (8%). The C14 variant, on the other hand, only performed best for 3% of the global area which was mostly limited to land regions. Among all models, the standalone model of Abramowitz et al. (2012) ("A12") exhibited the lowest RMSE over the second largest proportion of area (18%). That 17.5% of this 18% occurred over ocean is a surprising result given that the model was developed for application on land.

Figure 1e shows the spatial pattern in RMSE for the best performing variant on land, that is, CSCM & B32-CS. RMSEs approaching 40 W m^{-2} appeared in the marine coastal regions off western N. America, western north Africa, western south Africa, eastern S. America, and the entire Mediterranean region. These were notably reduced when the new CSCM was applied instead together with the S&R21 clear-sky model (Figure 1f, blue regions), likely owed to a reduced redundancy in input variables among the two models. These reductions, however, came at the expense of large RMSE increases in several regions (Figure 1f, red regions)—notably in the southeast Pacific Ocean region and in the arid regions of the Middle East, north Africa, and northeast Asia.

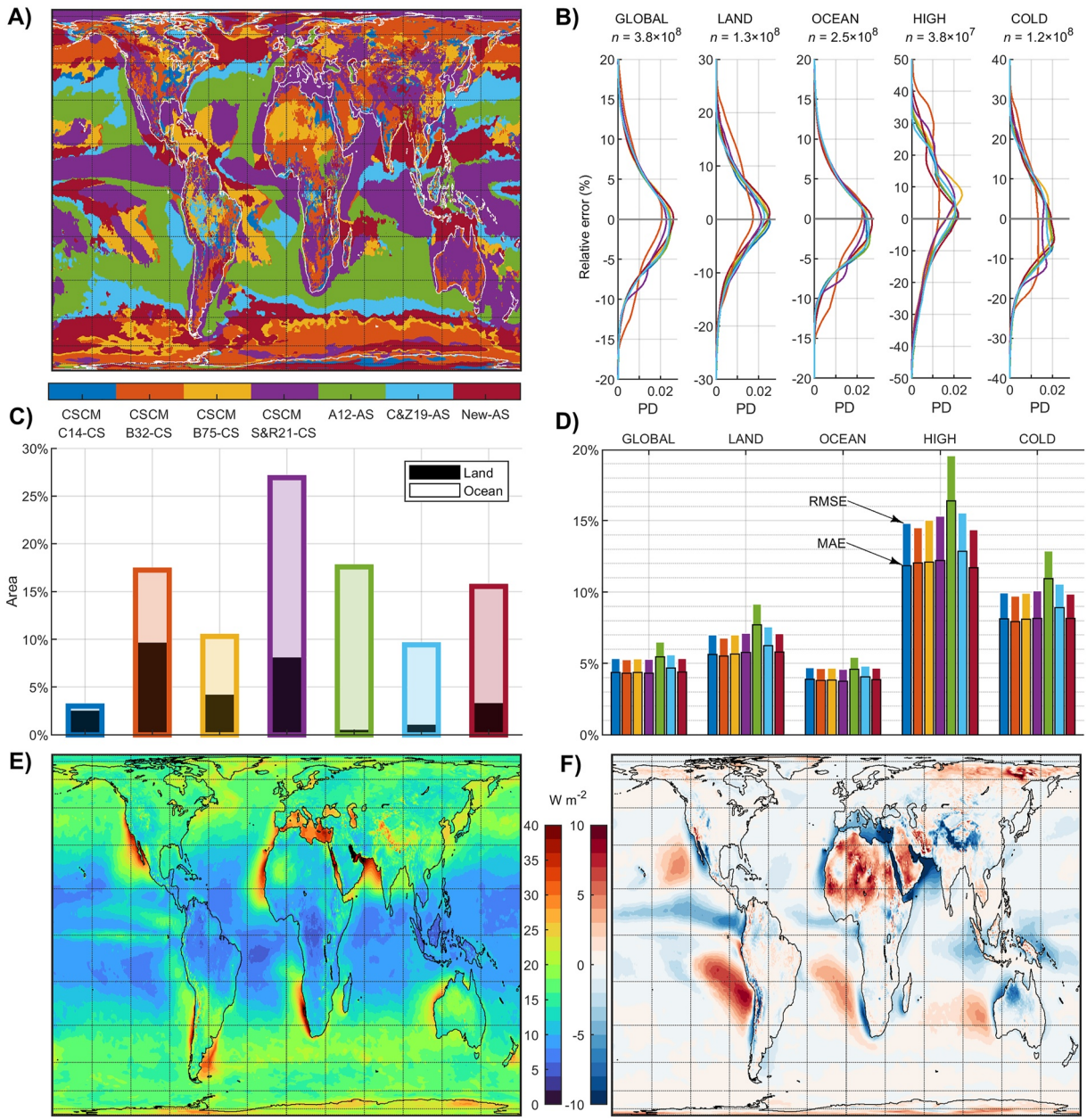

Figure 1. Performances based on ERA5; (a) Best model (lowest root mean squared error (RMSE)); (b) Probability densities ("PD") of relative error by model and subset; (c) Proportion of global area yielding the lowest RMSE by model—or the sum of the areas seen in panel (a) relative to Earth's total surface area; (d) Relative RMSE and mean absolute error (MAE) by model and subset–or the absolute RMSEs/MAEs divided by the subset mean observation; (e) RMSE of the best cloud-free model over land (CSCM & B32-CS); (f) Difference in RMSE between the best model over ocean and land (Δ = CSCM & S&R21-CS − CSCM & B32-CS). Note that panels (a–d) share the same color mapping. ERA5 subset means (in W m^{-2}) used to calculate metrics in panel (d) are: "GLOBAL" = 305; "LAND" = 253; "OCEAN" = 332; "ALT" = 147; "COLD" = 194.

Shifting to the *in-situ* performance results (Figure 2), model rankings were in broad agreement with those of the ERA5 LAND subset at comparable flux magnitudes (Figure 2a; 255 W m^{-2}). MAEs for the four CSCM variants and the new standalone model ("New-AS") were lower (~6.5–7%) than those of the C&Z19 (~7.5%) and A12 (~9.5%) models. Relative MAEs evaluated at the mean observation magnitude of the full data set clustered around 4.5% for the CSCM variants and the new standalone model. The superiority of these models was evident over the magnitude range ~180–330 W m^{-2}, prior to and after which errors from C&Z19 were found to be comparable. Only at magnitudes above ~380 W m^{-2} did MAEs from A12 match or fall below those of the other models. Errors from the new CSCM variant employing B32 were lowest over the largest observation range–or

10.1029/2023GL103790

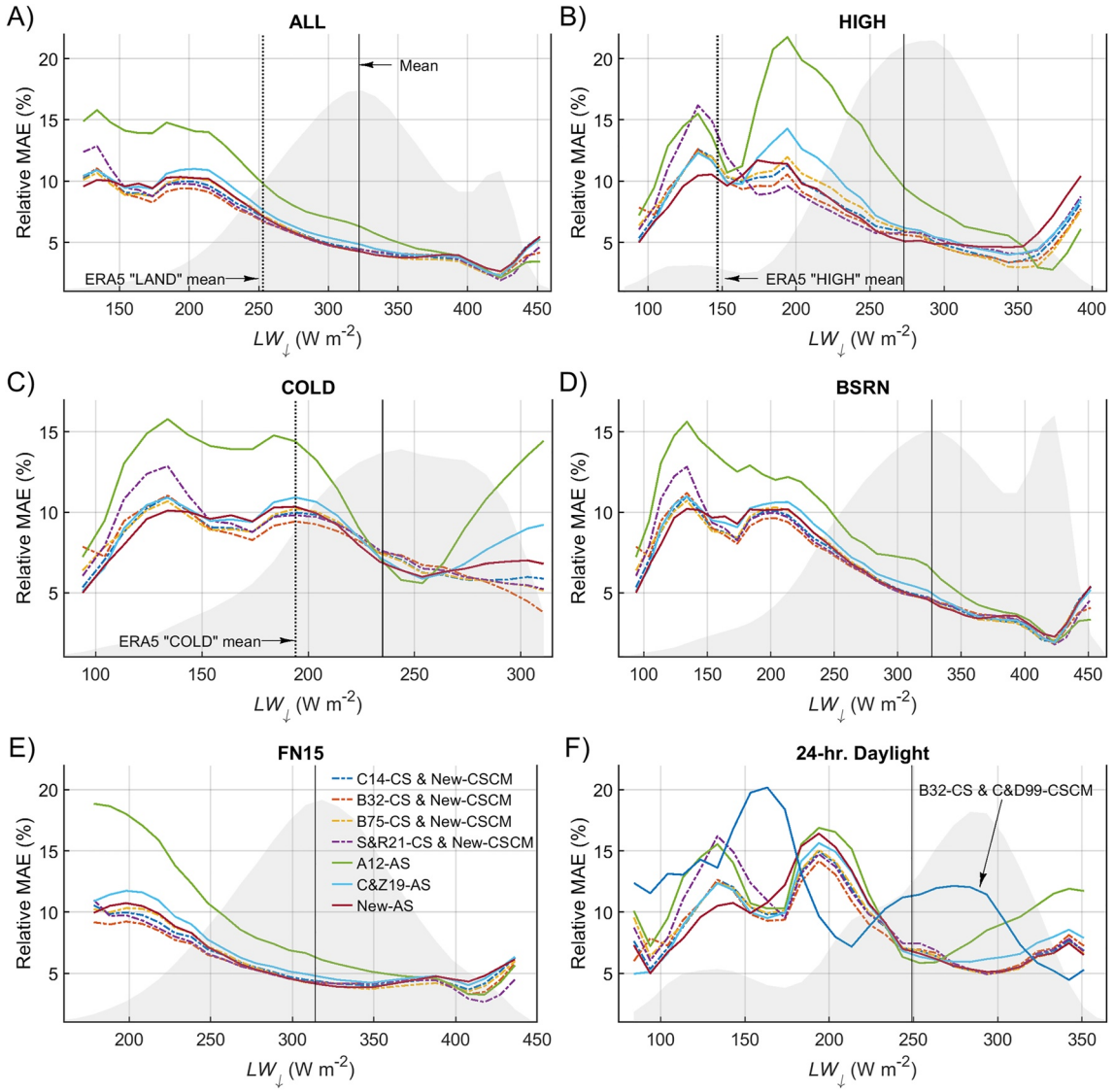

Figure 2. Relative mean absolute error (MAE) as a function of observation magnitude for the full land-based *in-situ* data set (a) and five subsets (b–f). Solid black vertical lines indicate the subset observation means used in relative MAE computation, while gray shaded areas indicate observation distributions (shapes only). "B32-CS & C&D99-CSCM" denotes the Crawford and Duchon (1999) correction model applied to the Brunt (1932) clear–sky model estimates.

~160–260 W m^{-2}. In general, MAE decreased with increasing flux magnitudes, in agreement with findings reported elsewhere (Gubler et al., 2012).

At higher altitudes (Figure 2b), MAEs of the new standalone model ("New-AS") were lowest of all models when evaluated at the observation subset mean (~5%) and ERA5 HIGH subset mean (~11%). Model rankings were however mixed when comparing MAEs over the full observation range, highlighting the limitations of non-locally parameterized parametric models when applied at high altitudes.

In colder environments (Figure 2c) the B32 CSCM variant emerged best over the largest observation range (~160–215 and ~280–315 W m^{-2}) and its MAE agreed well with that from the ERA5-based performance analysis (Figure 2b) when evaluated at the mean observation of the ERA5 COLD subset—or ~8%. Interestingly, lowest MAEs were found for the A12 model over the most frequent observation range spanning ~240–255 W m^{-2} although the reason is unclear.

Model rankings and MAEs were generally agreeable between the BSRN (Figure 2d) and FN15 (Figure 2e) subsets. A notable exception is the observation range of ~90–180 W m^{-2} for the BSRN subset where the S&R21-based CSCM variant yielded the second highest MAE after the A12 model.

Relative to the Crawford and Duchon (1999) CSCM applied to B32, the new CSCM applied to B32 yielded notably lower MAEs over a large observation range for the 24-hr daylight subset (Figure 2f)—which is the only subset allowing such a comparison. The MAE when evaluated at the subset mean was 12% for the former, in contrast to 7% yielded by the latter.

5. Discussion

The new "cloud-free" CSCM with its globally calibrated parameters performed remarkably well considering its simplicity, outperforming existing standalone models and the f_c*-based CSCM of Crawford and Duchon (1999). Performance differences among the four CSCM variants were small and owed to differences in their parameter sets, which may have compensated for systematic errors of the underlying clear-sky models. Although differences were slight, the new CSCM parameterized to the Brunt (1932) clear-sky model (henceforth "CSCM-B32") yielded both the lowest RMSE and MAE over both the full ERA5 and *in-situ* validation datasets. Of the four variants, CSCM-B32 yielded the lowest RMSE at three out of four ERA5 subsets (Figure 1d) and at four out of five *in-situ* subsets (Table S4 in Supporting Information S1), while yielding the lowest MAE at two of the four ERA5 subsets and four of five *in-situ* datasets (Table S4 in Supporting Information S1).

The superiority of this variant was attributed to the superiority of the B32-CS model itself which gave the lowest RMSE and MAE at three of the four ERA5 validation subsets (Table S3 in Supporting Information S1). The Shakespeare and Roderick (2021) model ("S&R21-CS") gave better clear-sky estimates at the OCEAN subset, which translated to better all-sky estimates at the same subset when applied together with the new CSCM. That the S&R21-CS model did not emerge best at other subsets was surprising given its stronger physical basis. In fact, in terms of both RMSE and MAE, the parametric model of Carmona et al. (2014) ("C14-CS") performed better overall and at all subsets except OCEAN relative to S&R21-CS—a finding that does not align with those reported in Shakespeare and Roderick (2021), possibly owed to differences in temporal resolution (hourly vs. daily) and/or use of different C14-CS model parameters calibrated on a significantly smaller data set.

As a true daily model with globally tuned parameters, it is difficult to benchmark the performance of CSCM-B32 against that of other models reported elsewhere for three reasons: (a) performance metrics often relate to daily averages calculated from hourly estimates; (b) other models are typically only evaluated locally or regionally using locally- (or regionally) calibrated parameters; (c) absolute rather than relative performance metrics are often reported without the observation means required to re-scale them across different validation datasets.

Nevertheless, RMSEs of 17.2 and 18.8 W m^{-2} yielded by CSCM-B32 for the ERA5 LAND and *in-situ* datasets, respectively, are on par with the 17.8 W m^{-2} RMSE reported by Feng et al. (2021) for their gradient boosting regression tree model which uses land-optimized parameters and additional input variables such as daily total column water vapor, solar irradiance, and elevation.

In cold environments ("COLD" subsets), RMSEs from CSCM-B32 were 9% (20.8 W m^{-2}) and 10% (18.9 W m^{-2}) for *in-situ* and ERA5 datasets, respectively. This is comparable to the ∼8–10% (19–22 W m^{-2}) range reported in Chiacchio et al. (2002) for all-sky estimates at two Arctic locations based on eight correction models with locally calibrated parameters and daily inputs—some of which employing multiple cloud variables derived from satellites and ceilometers.

As for CSCMs employing solar-derived cloud fraction or cloudiness proxies (f_c*) calculated at the sub-daily resolution, performances reported in literature varied widely depending on location and on the assumptions adopted when scaling to the daily resolution. When the daytime mean f_c* was assumed as the daily mean, Flerchinger et al. (2009) reported daily RMSEs across seven sites in the conterminous United States ranging from 15.7 to 20.6 W m^{-2} depending on the underlying clear-sky-correction model combination. When the daytime mean f_c* based on hourly averaged f_c* was assumed as the daily mean, Li et al. (2017) reported a daily RMSE of 6.7% for the Crawford and Duchon (1999) CSCM applied to a regionally calibrated B32-CS estimate which is higher than our finding of 5.8% (*in-situ* results) for the new CSCM applied to a *globally* calibrated B32-CS model estimate. The fact that errors from these regionally calibrated approaches based on f_c* were as high or higher than our globally calibrated modeling approach circumventing f_c* supports the assertion by Gubler et al. (2012) that f_c*-based approaches are too error prone given the high sensitivity of f_c* to modeled fractional clear-sky solar irradiances (i.e., the variable "*s*" in Crawford and Duchon (1999)—or $SW_{\downarrow}/SW_{0\downarrow}$).

6. Concluding Remarks

Given its simplicity, the proposed CSCM and its globally calibrated parameters shows promise as a true daily and universally applicable model based on standard meteorological inputs, with accuracies that appear to meet and even exceed those of prevailing modeling approaches employing regionally optimized parameters. Irrespective of the underlying clear-sky model, daily errors (RMSE) from the new correction are lower than those reported for many satellite-based algorithms (Riihelä et al., 2017; Tang et al., 2021; Zeng et al., 2020). Future research efforts might be directed toward examining modifications that lead to performance enhancements in cold and high-altitude environments.

Conflict of Interest

The authors declare no conflicts of interest relevant to this study.

Data Availability Statement

The FLUXNET15 data set is available from: https://fluxnet.org/data/fluxnet2015-dataset/. The BSRN data are available from: https://bsrn.awi.de/data/conditions-of-data-release/. The ERA5 data are available from: https://cds.climate.copernicus.eu/cdsapp#!/dataset/reanalysis-era5-single-levels?tab=overview.

Acknowledgments
Support was provided by the Research Council of Norway, Grants 295128 (R.M.B. and S.E.) and 342631/L10 (R.M.B.).

References

Abramowitz, G., Pouyanné, L., & Ajami, H. (2012). On the information content of surface meteorology for downward atmospheric long-wave radiation synthesis. *Geophysical Research Letters*, *39*(4). https://doi.org/10.1029/2011gl050726

Arking, A. (1991). The radiative effects of clouds and their impact on climate. *Bulletin of the American Meteorological Society*, *72*(6), 795–814. https://doi.org/10.1175/1520-0477(1991)072<0795:treoca>2.0.co;2

Bojinski, S., Verstraete, M., Peterson, T. C., Richter, C., Simmons, A., & Zemp, M. (2014). The concept of essential climate variables in support of climate research, applications, and policy. *Bulletin of the American Meteorological Society*, *95*(9), 1431–1443. https://doi.org/10.1175/bams-d-13-00047.1

Brunt, D. (1932). Notes on radiation in the atmosphere. I. *Quarterly Journal of the Royal Meteorological Society*, *58*(247), 389–420. https://doi.org/10.1002/qj.49705824704

Brutsaert, W. (1975). On a derivable formula for long-wave radiation from clear skies. *Water Resources Research*, *11*(5), 742–744. https://doi.org/10.1029/wr011i005p00742

Buck, A. L. (1981). New equations for computing vapor pressure and enhancement factor. *Journal of Applied Meteorology and Climatology*, *20*(12), 1527–1532. https://doi.org/10.1175/1520-0450(1981)020<1527:nefcvp>2.0.co;2

Carmona, F., Rivas, R., & Caselles, V. (2014). Estimation of daytime downward longwave radiation under clear and cloudy skies conditions over a sub-humid region. *Theoretical and Applied Climatology*, *115*(1), 281–295. https://doi.org/10.1007/s00704-013-0891-3

Castro Aguilar, J. L., Gentle, A. R., Smith, G. B., & Chen, D. (2015). A method to measure total atmospheric long-wave down-welling radiation using a low cost infrared thermometer tilted to the vertical. *Energy*, *81*, 233–244. https://doi.org/10.1016/j.energy.2014.12.035

Chang, K., & Zhang, Q. (2019). Modeling of downward longwave radiation and radiative cooling potential in China. *Journal of Renewable and Sustainable Energy*, *11*(6), 066501. https://doi.org/10.1063/1.5117319

Cheng, J., Yang, F., & Guo, Y. (2019). A comparative study of bulk parameterization schemes for estimating cloudy-sky surface downward long-wave radiation. *Remote Sensing*, *11*(5), 528. https://doi.org/10.3390/rs11050528

Chepfer, H., Brogniez, H., & Noel, V. (2019). Diurnal variations of cloud and relative humidity profiles across the tropics. *Scientific Reports*, *9*(1), 16045. https://doi.org/10.1038/s41598-019-52437-6

Chiacchio, M., Francis, J., & Stackhouse, P. (2002). Evaluation of methods to estimate the surface downwelling longwave flux during Arctic winter. *Journal of Applied Meteorology*, *41*(3), 306–318. https://doi.org/10.1175/1520-0450(2002)041<0306:eomtet>2.0.co;2

Choi, M. (2013). Parameterizing daytime downward longwave radiation in two Korean regional flux monitoring network sites. *Journal of Hydrology*, *476*, 257–264. https://doi.org/10.1016/j.jhydrol.2012.10.041

Cox, D. T. C., Maclean, I. M. D., Gardner, A. S., & Gaston, K. J. (2020). Global variation in diurnal asymmetry in temperature, cloud cover, specific humidity and precipitation and its association with leaf area index. *Global Change Biology*, *26*(12), 7099–7111. https://doi.org/10.1111/gcb.15336

Crawford, T. M., & Duchon, C. E. (1999). An improved parameterization for estimating effective atmospheric emissivity for use in calculating daytime downwelling longwave radiation. *Journal of Applied Meteorology*, *38*(4), 474–480. https://doi.org/10.1175/1520-0450(1999)038<0474:aipfee>2.0.co;2

Dai, A., Trenberth, K. E., & Karl, T. R. (1999). Effects of clouds, soil moisture, precipitation, and water vapor on diurnal temperature range. *Journal of Climate*, *12*(8), 2451–2473. https://doi.org/10.1175/1520-0442(1999)012<2451:eocsmp>2.0.co;2

di Sarra, A., Bommarito, C., Anello, F., Di Iorio, T., Meloni, D., Monteleone, F., et al. (2019). Assessing the quality of shortwave and longwave irradiance observations over the ocean: One year of high-time-resolution measurements at the Lampedusa Oceanographic Observatory. *Journal of Atmospheric and Oceanic Technology*, *36*(12), 2383–2400. https://doi.org/10.1175/jtech-d-19-0018.1

Driemel, A., Augustine, J., Behrens, K., Colle, S., Cox, C., Cuevas-Agulló, E., et al. (2018). Baseline surface radiation network (BSRN): Structure and data description (1992–2017). *Earth System Science Data*, *10*(3), 1491–1501. https://doi.org/10.5194/essd-10-1491-2018

Duarte, H. F., Dias, N. L., & Maggiotto, S. R. (2006). Assessing daytime downward longwave radiation estimates for clear and cloudy skies in Southern Brazil. *Agricultural and Forest Meteorology*, *139*(3), 171–181. https://doi.org/10.1016/j.agrformet.2006.06.008

Feng, C., Zhang, X., Wei, Y., Zhang, W., Hou, N., Xu, J., et al. (2021). Estimation of long-term surface downward longwave radiation over the global land from 2000 to 2018. *Remote Sensing*, *13*(9), 1848. https://doi.org/10.3390/rs13091848

Flerchinger, G. N., Xaio, W., Marks, D., Sauer, T. J., & Yu, Q. (2009). Comparison of algorithms for incoming atmospheric long-wave radiation. *Water Resources Research*, *45*(3). https://doi.org/10.1029/2008wr007394

Ghate, V. P., Albrecht, B. A., Fairall, C. W., & Weller, R. A. (2009). Climatology of surface meteorology, surface fluxes, cloud fraction, and radiative forcing over the Southeast Pacific from Buoy observations. *Journal of Climate*, *22*(20), 5527–5540. https://doi.org/10.1175/2009jcli2961.1

Gubler, S., Gruber, S., & Purves, R. S. (2012). Uncertainties of parameterized surface downward clear-sky shortwave and all-sky longwave radiation. *Atmospheric Chemistry and Physics*, *12*(11), 5077–5098. https://doi.org/10.5194/acp-12-5077-2012

Guo, Y., Cheng, J., & Liang, S. (2019). Comprehensive assessment of parameterization methods for estimating clear-sky surface downward longwave radiation. *Theoretical and Applied Climatology*, *135*(3), 1045–1058. https://doi.org/10.1007/s00704-018-2423-7

Hersbach, H., Bell, B., Berrisford, P., Hirahara, S., Horányi, A., Muñoz-Sabater, J., et al. (2020). The ERA5 global reanalysis. *Quarterly Journal of the Royal Meteorological Society*, *146*(730), 1999–2049. https://doi.org/10.1002/qj.3803

Kondratyev, K. Y. (1969). *Radiation in the atmosphere* (p. 912). Academic Press.

Konzelmann, T., van de Wal, R. S. W., Greuell, W., Bintanja, R., Henneken, E. A. C., & Abe-Ouchi, A. (1994). Parameterization of global and longwave incoming radiation for the Greenland Ice Sheet. *Global and Planetary Change*, *9*(1), 143–164. https://doi.org/10.1016/0921-8181(94)90013-2

Letu, H., Nakajima, T. Y., Wang, T., Shang, H., Ma, R., Yang, K., et al. (2022). A new benchmark for surface radiation products over the East Asia–Pacific region retrieved from the Himawari-8/AHI Next-Generation Geostationary Satellite. *Bulletin of the American Meteorological Society*, *103*(3), E873–E888. https://doi.org/10.1175/bams-d-20-0148.1

Lhomme, J. P., Vacher, J. J., & Rocheteau, A. (2007). Estimating downward long-wave radiation on the Andean Altiplano. *Agricultural and Forest Meteorology*, *145*(3), 139–148. https://doi.org/10.1016/j.agrformet.2007.04.007

Li, M., Jiang, Y., & Coimbra, C. F. M. (2017). On the determination of atmospheric longwave irradiance under all-sky conditions. *Solar Energy*, *144*, 40–48. https://doi.org/10.1016/j.solener.2017.01.006

Liu, L., Zhang, T., Wu, Y., Niu, Z., & Wang, Q. (2018). Cloud effective emissivity retrievals using combined ground-based infrared cloud measuring instrument and ceilometer observations. *Remote Sensing*, *10*(12), 2033. https://doi.org/10.3390/rs10122033

Marty, C., & Philipona, R. (2000). The clear-sky index to separate clear-sky from cloudy-sky situations in climate research. *Geophysical Research Letters*, *27*(17), 2649–2652. https://doi.org/10.1029/2000gl011743

Pastorello, G., Trotta, C., Canfora, E., Chu, H., Christianson, D., Cheah, Y. W., et al. (2020). The FLUXNET2015 dataset and the ONEFlux processing pipeline for eddy covariance data. *Scientific Data*, *7*(1), 225. https://doi.org/10.1038/s41597-020-0534-3

Pirazzini, R., Nardino, M., Orsini, A., Calzolari, F., Georgiadis, T., & Levizzani, V. (2000). Parameterization of the downward longwave radiation from clear and cloudy skies at Ny Ålesund (Svalbard). In W. L. Smith & Y. A. Timofeyev (Eds.), *IRS2000: Current problems in atmospheric radiation* (pp. 559–562). A. Deepak Publishing.

Riihelä, A., Key, J. R., Meirink, J. F., Kuipers Munneke, P., Palo, T., & Karlsson, K.-G. (2017). An intercomparison and validation of satellite-based surface radiative energy flux estimates over the Arctic. *Journal of Geophysical Research: Atmospheres*, *122*(9), 4829–4848. https://doi.org/10.1002/2016jd026443

Rutan, D. A., Kato, S., Doelling, D. R., Rose, F. G., Nguyen, L. T., Caldwell, T. E., & Loeb, N. G. (2015). CERES synoptic product: Methodology and validation of surface radiant flux. *Journal of Atmospheric and Oceanic Technology*, *32*(6), 1121–1143. https://doi.org/10.1175/jtech-d-14-00165.1

Shakespeare, C. J., & Roderick, M. L. (2021). The clear-sky downwelling long-wave radiation at the surface in current and future climates. *Quarterly Journal of the Royal Meteorological Society*, *147*(741), 4251–4268. https://doi.org/10.1002/qj.4176

Sicart, J. E., Pomeroy, J. W., Essery, R. L. H., & Bewley, D. (2006). Incoming longwave radiation to melting snow: Observations, sensitivity and estimation in northern environments. *Hydrological Processes*, *20*(17), 3697–3708. https://doi.org/10.1002/hyp.6383

Sridhar, V., & Elliott, R. L. (2002). On the development of a simple downwelling longwave radiation scheme. *Agricultural and Forest Meteorology*, *112*(3), 237–243. https://doi.org/10.1016/s0168-1923(02)00129-6

Sundqvist, H. (1978). A parameterization scheme for non-convective condensation including prediction of cloud water content. *Quarterly Journal of the Royal Meteorological Society*, *104*(441), 677–690. https://doi.org/10.1002/qj.49710444110

Tang, W., Qin, J., Yang, K., Zhu, F., & Zhou, X. (2021). Does ERA5 outperform satellite products in estimating atmospheric downward longwave radiation at the surface? *Atmospheric Research*, *252*, 105453. https://doi.org/10.1016/j.atmosres.2021.105453

Walcek, C. J. (1994). Cloud cover and its relationship to relative humidity during a springtime midlatitude cyclone. *Monthly Weather Review*, *122*(6), 1021–1035. https://doi.org/10.1175/1520-0493(1994)122<1021:ccairt>2.0.co;2

Wang, K., & Dickinson, R. E. (2013). Global atmospheric downward longwave radiation at the surface from ground-based observations, satellite retrievals, and reanalyses. *Reviews of Geophysics*, *51*(2), 150–185. https://doi.org/10.1002/rog.20009

Wang, K., & Liang, S. (2009). Global atmospheric downward longwave radiation over land surface under all-sky conditions from 1973 to 2008. *Journal of Geophysical Research*, *114*(19), D19101. https://doi.org/10.1029/2009jd011800

Wang, T., Shi, J., Ma, Y., Letu, H., & Li, X. (2020). All-sky longwave downward radiation from satellite measurements: General parameterizations based on LST, column water vapor and cloud top temperature. *ISPRS Journal of Photogrammetry and Remote Sensing*, *161*, 52–60. https://doi.org/10.1016/j.isprsjprs.2020.01.011

Yamanouchi, T., & Kawaguchi, S. (1984). Longwave radiation balance under a strong surface inversion in the katabatic wind zone, Antarctica, (pp. 11771–11778).

Yang, K., He, J., Tang, W., Qin, J., & Cheng, C. C. K. (2010). On downward shortwave and longwave radiations over high altitude regions: Observation and modeling in the Tibetan Plateau. *Agricultural and Forest Meteorology*, *150*(1), 38–46. https://doi.org/10.1016/j.agrformet.2009.08.004

Zeng, Q., Cheng, J., & Dong, L. (2020). Assessment of the long-term high-spatial-resolution Global LAnd Surface Satellite (GLASS) surface longwave radiation product using ground measurements. *IEEE Journal of Selected Topics in Applied Earth Observations and Remote Sensing*, *13*, 2032–2055. https://doi.org/10.1109/jstars.2020.2992472

References From the Supporting Information

Iziomon, M. G., Mayer, H., & Matzarakis, A. (2003). Downward atmospheric longwave irradiance under clear and cloudy skies: Measurement and parameterization. *Journal of Atmospheric and Solar-Terrestrial Physics*, *65*(10), 1107–1116. https://doi.org/10.1016/j.jastp.2003.07.007

Kjaersgaard, J. H., Plauborg, F. L., & Hansen, S. (2007). Comparison of models for calculating daytime long-wave irradiance using long term data set. *Agricultural and Forest Meteorology*, *143*(1), 49–63. https://doi.org/10.1016/j.agrformet.2006.11.007